Journal of Building Engineering 50 (2022) 104159

Contents lists available at ScienceDirect

Journal of Building Engineering

journal homepage: www.elsevier.com/locate/jobe

Real-time optimal control of HVAC systems: Model accuracy and optimization reward

Jin Hou [a], Xin Li [a], Hang Wan [a], Qin Sun [b], Kaijun Dong [b], Gongsheng Huang [a,*]

[a] Department of Architecture and Civil Engineering, City University of Hong Kong, Kowloon, Hong Kong
[b] Guangzhou Instituted of Energy Conversion and Key Laboratory of Renewable Energy, Chinese Academy of Sciences, Guangzhou, 510665, China

ARTICLE INFO

Keywords:
Real-time optimal control
Reward of optimization action
Event-driven optimization
Air-conditioning system
Building energy efficiency

ABSTRACT

Real-time optimal control is considered as an efficient tool to improve the energy efficiency of heating, ventilation, and air-conditioning (HVAC) systems. It minimizes the energy consumption of HVAC systems by searching the optimal settings (normally set-points) for local control loops. Generally, in a model-based real-time optimal control, a reliable and accurate model is important for optimization performance but not easy to be obtained in practice. Thus, model errors exist universally and cannot be avoided in the application. The model error may have a negative impact on the performance of real-time optimal control. For example, in power minimization, some individual optimization actions may lead to power use increase (negative reward) instead of power use decrease (positive reward). This paper analyzes the impact of model accuracy on individual optimization actions. Using numerical analysis, different sizes of model accuracy were investigated and the possibility of positive/negative reward was quantified in percentage. This paper also revealed that event-based optimal control with controlled thresholds could significantly reduce the percentage of negative reward when compared with a time-based optimal control (e.g. optimization was carried out every 30 min).

1. Introduction

Control is essential for the operation of HVAC systems, which can be basically categorized into local (process) control and supervisory/optimal control [1]. The former is used to track predefined set points for local processes [2], such as supply air temperature control of air-handling unit and room temperature control. There are many algorithms developed for local process control, such as classical PI/PID [2], fuzzy control [3] and recently developed model-based predictive control [4] or robust control [5]. The latter is always utilized online to monitor/adjust the set-points (or other settings) for local controls, aiming at minimize the energy consumption or the operational cost of HVAC systems [1,6,7].

Current literature has demonstrated that real-time optimal control (RTOC), as a supervisor control, is an efficient tool to improve the energy efficiency of HVAC systems [1,7]. RTOC has undergone rapid development since the 1980s [8], and its framework for HVAC systems has been well established, which has the basic elements of decision variable, cost function, constraint, optimizer searching technique, and/or system/component model [9,10]. The energy use, power consumption or operational cost of HVAC systems are always used as the cost functions to be minimized or maximized. Constraints refer to the limitations on the operation of systems, for example feasible temperature range, maximum or minimum flow rates. Optimizer searching techniques, such as evolutionary

* Corresponding author.
E-mail address: gongsheng.huang@cityu.edu.hk (G. Huang).

https://doi.org/10.1016/j.jobe.2022.104159
Received 20 September 2021; Received in revised form 21 January 2022; Accepted 31 January 2022
Available online 3 February 2022

algorithms [11–13], branch and bound [14], nonlinear programming [15], and simulated annealing [16], are adopted to search the values of decision variables that minimize or maximize the cost functions.

When the models of HVAC systems are used in a RTOC to describe the relationship between the decision variables (such as set points for local control loops) and the cost function, this RTOC is categorized as a model-based RTOC [17–19]. There are three types of models commonly used in the RTOC of HVAC systems: white-box (physical), black-box (data-driven), and gray-box (simplified semi-physical) models [7]. For example, physical building/plant models were used in the optimal control of a renewable energy system [20], where the net external energy consumption in the system operation was minimized. Li et al. developed a gray-box model for zones, based on which optimal control was able to achieve significant energy saving and improve the indoor environment simultaneously [21]. Amarasinghe et al. developed an artificial-neural-network (ANN) model to minimize the operating cost of thermal storage tanks in buildings [22]; while Afram et al. developed a black-box model to achieve the same target [23]. To improve the accuracy of component/system models, adaptive modeling (self-tuning modeling) was also proposed [24,25]. For example, Asad et al. proposed an adaptive modeling approach for RTOC of complex air-conditioning systems [25], in which a hybrid genetic algorithm was used to estimate and update model parameters using newly generated operation data.

Although various models are available at present and great efforts have already been paid to increase model accuracy, model errors exist universally and cannot be avoided in practice [26,27]. Model error can be defined as the difference between the actual value and the value predicted using the models of systems, which occurs due to model structure mismatch (e.g. linearization of nonlinear processes) [28], model parameter mismatch (e.g. poor quality of data for model training) [29], and model input uncertainty (e.g. noises and drafts in model input measurements) [30]. In a model-based RTOC, model error may lead to deviation of the actual value of the cost function from its predicted value, and thus the optimal solutions obtained from the model-based RTOC may not be truly 'optimal' for real operational conditions. A number of studies analyzed the impact of model errors on the performance of the RTOC of HVAC systems quantitatively. For example, Liu and Henze investigated building modeling mismatch and its impact on the performance of a model-based predictive optimal control of active and passive building thermal storage [31], and concluded that several categories of modeling mismatches, such as the mismatch in building construction characteristics and thermal energy storage (TES) performance, had a significant impact on the optimal control performance. Jiang and Reddy presented an approach for dynamic scheduling and optimal control of complex primary HVAC&R plants, the robustness of which to various sources of uncertainties was evaluated against a non-optimal approach [32]. These studies evaluated the impact of model errors on the overall performance of the optimization, but lack depth investigations on how model error affects individual optimization actions.

To investigate the impact of model error on individual optimization actions, optimization rewards need to be defined. When an optimization action leads to the expected enhancement in a specified performance index, this optimization action is considered to have a positive reward; otherwise, it has a negative reward. Due to model error, optimization actions could not always have a positive reward. For example, when a model-based RTOC is used to minimize the power of a HVAC system, the power might not be reduced as expected at each time instant. This is because the optimal values of the decision variables is calculated using a performance model and they are optimal for the model, but might not be optimal for the real system (details should refer to Fig. 1 in Section 2.1). Optimization actions with negative rewards should be avoided for enhancing the performance of optimization.

This paper investigated the impact of model errors on the individual optimization actions in a model-based RTOC of a typical air-conditioning system, where two driving mechanisms for optimization were considered: time-driven and event-driven. In the time-driven mechanism, the optimization action was activated by time, i.e. the optimization was performed with a constant frequency. While in the event-driven mechanism, the optimization was performed only when an event occurred [33,34]. Model errors from model parameter mismatch were focused in this study because gray-box models of HVAC systems were used to formulate the optimization problem. In gray-box models, part of model parameters need to be identified using operation data, and thus model-parameter mismatch easily occurs. Considering the limitation of experimental resources, numerical analysis was adopted. Using numerical analysis, different scales of model errors were investigated and the possibility of positive/negative reward was quantified in percentage. It was assumed that the air-conditioning system under consideration had no significant storage, and thus both the time-driven and event driven optimal control strategies belonged to static optimization [1]. Therefore, the optimization problem was formulated to minimize the instantaneous power of the air-conditioning system instead of energy use, which was different from dynamic optimal control strategies, such as those based on model predictive control (MPC) [35,36]. This paper was organized as follows. Theoretical background on positive/negative rewards of optimization actions and real-time optimal control was given in Section 2. Section 3 illustrated the methodology. Section 4 and Section 5 presented the numerical studies on the time-driven and event-driven optimization control of the air-conditioning systems respectively. Concluding remarks were given in Section 6.

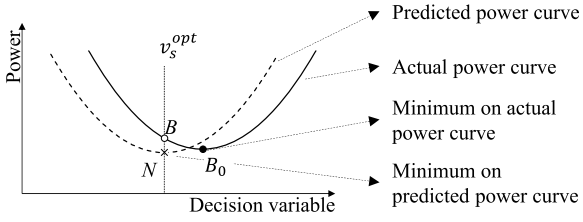

Fig. 1. An example to illustrate the influence of model errors on model-based optimal control under a certain operating condition.

2. Theoretical background

2.1. Positive/negative reward of optimization actions

The impact of model errors on the optimization is illustrated in Fig. 1, where the instantaneous power P of an air-conditioning system is minimized by optimizing a decision variable v under different operating conditions. Given an operation condition, which is described by a state vector S, different values of the decision variable v yield different values of the power P. The variation of the power along with the decision variable is defined as the power curve corresponding to a state S. To find the optimal value of the decision variable, denoted as v_s^{opt}, a power prediction model should be used if a model-based optimal control strategy is adopted. The power curve, calculated using the power prediction model, is titled as *predicted power curve*. If the model is ideal, i.e. no model errors, the corresponding power curve is titled as an *actual power curve*. Due to model errors, the predicted power curve deviates from the actual power curve as shown in Fig. 1.

In the model-based optimal control, v_s^{opt} is identified according to the predicted power curve, and the corresponding expected power minimum P_N is at the point N. As a comparison, the actual power minimum P_{B_0} should be at the point B_0. When v_s^{opt} is applied to the system, the real power consumed by the system P_B should be at the point B instead of at the minimum B_0. The difference P_B and P_{B_0} indicates the influence of model errors on model-based optimization.

The reward of optimization under model errors is illustrated in Fig. 2. When the operating state changes from S_1 to S_2, the power curves, whether the actual or the predicted, change accordingly as shown by the darkened solid and dotted lines respectively. If optimization is done under the state S_2, the optimal value of the decision variable will be identified as $v_{S_2}^{opt}$ according to the predicted power curve. Similarly, the corresponding actual power happens at the point B, and the minimums on the predicted and actual power curve happen at the points N and B_0 respectively. If no optimization is done, $v_{S_1}^{opt}$ will be still used and the actual power will be at the point A. Thus, the optimization action under the state S_2 reduces the instantaneous power by ΔP_{AB}, defined by

$$\Delta P_{AB} = P_A - P_B \tag{1}$$

ΔP_{AB} could be positive, such as the one shown in Fig. 2(a), or negative, such as the one shown in Fig. 2(b). If ΔP_{AB} is positive, the power is reduced by the optimization; while if ΔP_{AB} is negative, the power is increased by the optimization, which indicates that the optimization is counterproductive.

Based on the above discussion, the reward of an optimization action can be defined as

$$ROpt = P_{opt} - \widetilde{P}_{nopt} \tag{2}$$

where P_{opt} is the power when the optimization action is performed, and $\widetilde{P}_{nopt}$ is the power when no optimization action is performed. When the optimization reward is negative, the optimization action will be detrimental to energy conservation, which should be avoided.

2.2. Real-time optimal control of air-conditioning systems

The schematic structure of a typical central air-conditioning system is given in Fig. 3. The system has three functional blocks: an air-handling unit (AHU) that cools down the supply air through the chilled water inside the cooling coil and supplies conditioned air to indoor spaces using supply air fans; a chiller unit that generates chilled water using a refrigeration cycle to transfer the heat from its evaporator side to condenser side; and a cooling tower unit that dissipates heat from the condenser of the chiller into the atmosphere. The water pump circulates the cooling water or chilled water in the corresponding water loops. The major power is consumed by the fans in the AHU $P_{AHU,f}$, the pumps in the chilled water primary and secondary loop $P_{ch,p}$, the compressors in the chiller $P_{ch,c}$, the pumps in the condenser water loop $P_{ct,p}$, and the fans in the cooling tower $P_{ct,f}$. Thus, the total power P_{tot} is

$$P_{tot} = P_{AHU,f} + P_{ch,p} + P_{ch,c} + P_{ct,p} + P_{ct,f} \tag{3}$$

The total instantaneous power P_{tot} of the system is a function of current weather condition, the cooling load, and the setting of local controls, which has the form of

$$P_{tot} = f\left(Cl, T_{db}, T_{wb}, T_{sa,st}, T_{chw,st}, T_{cw,st}\right) \tag{4}$$

where Cl is the cooling load; T_{db} and T_{wb} are the outdoor air dry bulb and wet bulb temperature respectively, representing weather

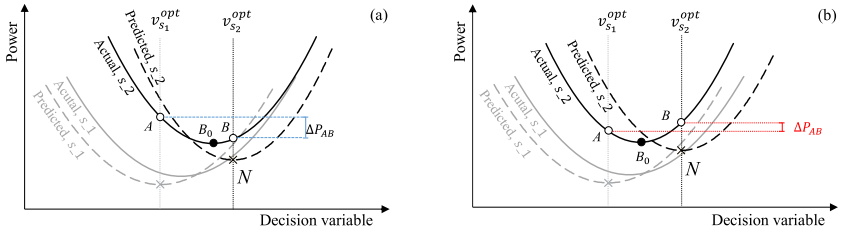

Fig. 2. Examples to illustrate the reward of optimization actions: (a) positive reward; (b) negative reward.

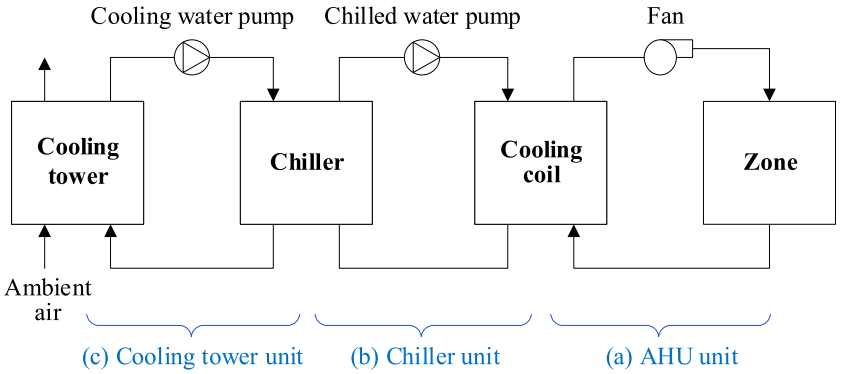

Fig. 3. The schematic structure of a typical central air-conditioning system: (a) air-handling unit; (b) chiller unit; and (c) cooling tower unit.

conditions; while $T_{sa,st}$, $T_{chw,st}$, and $T_{cw,st}$ are the set-points for the supply air temperature, chilled water supply temperature, and condenser water return temperature respectively, representing local control settings and being controlled by local controllers to follow their set-points.

Given Cl, T_{db} and T_{wb}, different combinations of $T_{sa,st}$, $T_{chw,st}$, and $T_{cw,st}$ lead to different P_{tot}, which provides the basis for real-time optimal control. The real-time optimization aims to seek the combination of the three decision variables that leads to the minimum power consumption under current operating states. Without significant thermal mass used in the system, the real-time optimal control of the air-conditioning systems is always formulated as

$$\left[T^{opt}_{cw,st}, T^{opt}_{chw,st}, T^{opt}_{sa,st}\right] = \min_{T_{sa,st}, T_{chw,st}, T_{cw,st}} P_{tot} \text{ subject to operation constraints} \tag{5}$$

where $T^{opt}_{cw,st}$, $T^{opt}_{chw,st}$, and $T^{opt}_{sa,st}$ denote the optimal values of $T_{sa,st}$, $T_{chw,st}$, and $T_{cw,st}$ respectively. The power P_{tot} can be calculated using various performance models developed for air-conditioning components, such as physical, gray-box or black-box models [1,12].

The two mechanisms that are used to activate optimization action are compared in Fig. 4. The top one shows the time-driven mechanism, while the bottom one shows the event-driven mechanism. It can be seen that the time-driven mechanism activates optimization action in a fixed frequency, for example the optimization being performed every 30 min. In the event-driven mechanism, optimization action is activated if certain events occur [33,34]. Events are generally defined based on the operating conditions of HVAC systems, such as the changes in Cl, T_{db} and T_{wb} [37], leading to more optimization actions when the operating conditions have significant changes and fewer actions when the operating conditions are stable.

3. Methodology

3.1. Overview of the methodology

Model errors will affect both the TDOC and the EDOC, resulting in positive or negative rewards. As model errors are difficult to predict due to the complexity of HVAC systems and operating conditions, numerical analysis is adopted to study the influences. The methodology is shown in Fig. 5. A simulation platform for an air-conditioning system was firstly constructed, where TRNSYS was used to simulate a virtual air-conditioning system and considered as the "actual" system. Its real-time optimal control algorithm was realized in MATLAB, where the models of the air-conditioning systems, where were used in the optimization and detailed in Appendix, were identified using the data generated from TRNSYS. The air-conditioning system and the optimal control algorithm communicated

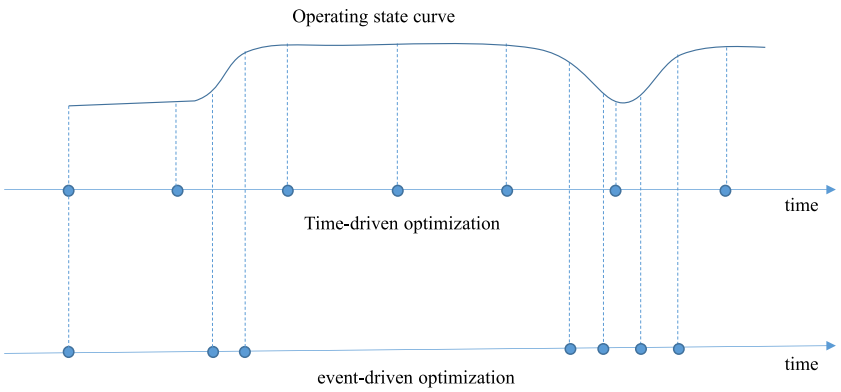

Fig. 4. Time-driven optimization vs event-driven optimization.

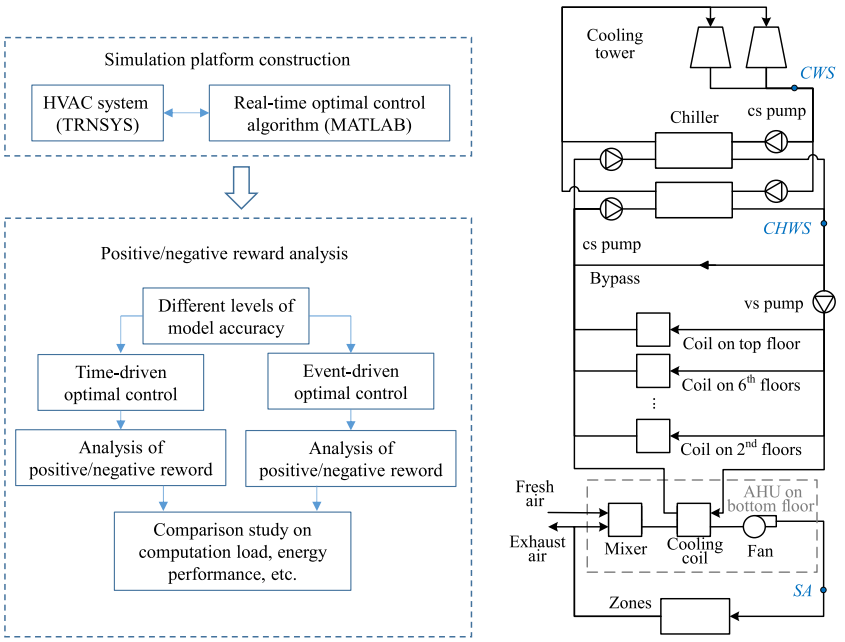

Fig. 5. The methodology adopted in this study (left); the schematic of the virtual air-conditioning system (right).

through the MATLAB interface provided by TRNSYS. Different levels of model errors were achieved by artificially adjusting the model parameters. The impact of model error on the TDOC approach was firstly analyzed and then on the TDOC. After that, a compassion study was carried out to demonstrate their different capacities to deal with model errors.

3.2. Simulation platform

An air-conditioning system that was used to cool a seven-story commercial building was adopted in this study. Its structure was

Table 1
Parameter settings of the components in TRNSYS.

Component	Number	Parameter	Value
Chiller (Type 666)	2	Capacity (kW)	480
		COP	6.5
		Chilled water flow rate (kg/s)	23
		Cooling water flow rate (kg/s)	27
Cooling tower (Type 51b)	2	Maximum air flow rate (m^3/s)	18
		Rated power (kW)	5
		Cooling water flow rate (kg/s)	27
		Cooling capacity (kW)	557
CHW cs pump (Type 114)	2	Water flowrate (kg/s)	23
		Head (m)	8
		Rated power (kW)	3
CW cs pump (Type 114)	2	Water flowrate (kg/s)	27
		Head (m)	10
		Rated power (kW)	4
CHW vs pump (Type 110)	1	Water flowrate (kg/s)	46
		Head (m)	26
		Rated power (kW)	18
AHU bottom floor	1		
Coil (Type 508c)		Coil bypass fraction	0.15
Fan (Type 111b)		Rated air flow rate (kg/s)	10
		Rated power (kW)	18.5
AHU middle floor	5		
Coil (Type 508c)		Coil bypass fraction	0.15
Fan (Type 111b)		Rated air flow rate (kg/s)	7
		Rated power (kW)	7
AHU top floor	1		
Coil (Type 508c)		Coil bypass fraction	0.15
Fan (Type 111b)		Rated air flow rate (kg/s)	8
		Rated power (kW)	10

illustrated in Fig. 5 (right), where two chillers coupled with two cooling towers were used to generate chilled water, and one air handling unit (AHU) was equipped on each floor to supply cooled air to the zones on this floor. The temperatures of the return cooling water, the supply chilled water, and the supply air were controlled to track their set-points by their corresponding local controllers. The type numbers of the system components in TRNSYS and their parameter settings were listed in Table 1. The rated capacity of the chiller was 480 kW with a rated coefficient of performance (COP) 6.5. The cooling tower with a rated cooling capacity of 557 kW was used to reject the heat from the condenser water. The rated water flowrates of the cooling water, the chilled water at the primary side, and the chilled water at the secondary side were 27 kg/s, 23 kg/s, and 46 kg/s respectively. The rated airflow rates of fans in AHUs on the top floor, middle floor, and bottom floor were 10 kg/s, 7 kg/s, and 8 kg/s, which were set according to their corresponding peak loads. Noted that the performance data in Type 666 (for the chillers) was rewritten according to a real chiller (Reform EIR Chiller Screw York YS 781kW/5.42COP/Valve), described in the software of DesignBuilder. The cooling load for the AHU on each floor was obtained through the load forecasting of a large office building of DOE'S commercial reference building models [38]. The cooling loads included all the amount contributed from the heat transfer through the building envelop, indoor heat source, and fresh air (fresh air ratio: 30%). The weather data for Hong Kong in EnergyPlus weather format [39] was used as the outdoor conditions for the building and its air-conditioning system.

The optimal control was used to minimize the total instantaneous power of the system, as illustrated in section 2.2. In the optimization formulated by Eqn. (3), the performance models of the system, where were used to calculate the system power P_{tot}, were given in Appendix I. All undetermined parameters of component models in the controller were identified using the data generated from the simulated system. In the optimization, these decision variables were constrained inside the range specified by Eqn. (6). An exhaustive search method was adopted to find the optimal solutions. A step change of 0.1 $^{\circ}C$ was used. The search ranges of the three decision variables were set as 1.4 $^{\circ}C$ as shown in Eqn. (7), which limited the set-point change between two adjacent time instants.

$$\begin{cases} T_{wb} + 1.5^{\circ}C \le T_{cw,st} \le 35^{\circ}C \\ 4^{\circ}C \le T_{chw,st} \le 10^{\circ}C \\ 12^{\circ}C \le T_{air,st} \le 16^{\circ}C \end{cases} \tag{6}$$

$$\begin{cases} \left|T_{cw,st,k} - T_{cw,st,k-1}\right| \le 1.4^{\circ}C \\ \left|T_{chw,st,k} - T_{chw,st,k-1}\right| \le 1.4^{\circ}C \\ \left|T_{sa,st,k} - T_{cw,sa,k-1}\right| \le 1.4^{\circ}C \end{cases} \tag{7}$$

The optimization reward defined in Eqn. (2) was calculated by the steps shown as follows. First, the system was optimized online using an optimization algorithm for a period of time. Denote the optimization time instants as $(t_1, t_2, \cdots, t_N)$, the corresponding optimal values of the decision variables as $(v_1^{opt}, v_2^{opt}, \cdots, v_N^{opt})$, and the optimized power as $(P_{opt,1}, P_{opt,2}, \cdots, P_{opt,N})$. Then, under the same environment, the system was running again with the sequence of $(v_0, v_1^{opt}, v_2^{opt}, \cdots, v_{N-1}^{opt})$ for the decision variables at the time instants $(t_1, t_2, \cdots, t_N)$, where v_0 is the default value for the decision variables. In this setting, the decision variables at t_k are not optimized, using v_{k-1}^{opt} instead of the optimal value v_k^{opt}. The corresponding power was denoted as $(\widetilde{P}_{nopt,1}, \widetilde{P}_{nopt,2}, \cdots, \widetilde{P}_{nopt,N})$. According to the definition in Eqn. (2), the optimization performed at the time k led to the reward as

$$Ropt_k = P_{opt,k} - \widetilde{P}_{nopt,k} \tag{8}$$

The values of $Ropt_k$ were used to analyze the optimization reward statistically.

4. Impact of model accuracy on time-driven optimal control

4.1. Time-based optimal control algorithm

With the cooling load and Hong Kong weather data as given in Table 3, the TDOC for the air-conditioning system was carried out for a week (July 1 to July 7). Four different optimization frequencies, namely every 15min, 30min, 60min, and 120min, were adopted for the TDOC. In total 1,260 sets of data at optimization time were collected.

To study the impact of model errors on the reward of optimization actions, the parameters of the component models in Table 2 were adjusted to make the model errors vary from the minimum (Case 1) to the maximum (Case 8). Four error indexes defined in Eqn.s (9)–(12) were used to describe the scale of model errors [43–47]. Among them, AE_{max} is the maximal value of the absolute error, where y^* is the predicted by the models and y the actual value. ARE_{max} is the maximum of the absolute relative error. RMSE is the root mean square error, indicating the quadratic mean of the differences between the predicted and the actual values. CV is the normalized value of the root mean square errors. In Table 4, y refers to the instantaneous power of the air-conditioning system.

Table 2
Models of components for calculating the system power (with details in Appendix I).

Component	Model
Chiller	DOE2 in Hydeman and Gillespie's study [40]
Cooling tower	Simplified cooling tower model in Lebrun et al.'s study [41]
Air handling unit	Type 508c in TRNSYS TESS [42]
variable speed pump	The cubic polynomial of fluid flowrate
Fan	The cubic polynomial of fluid flowrate

Table 3
Weather and load conditions.

Item		Max.	Min.	Mean
Db temp. (°C)		32.8	25.7	28.9
Wb temp. (°C)		27.3	23.8	25.8
Cooling load (kW)	Bottom floors	159.1	34.7	87.4
	Middle floors	117.4	38.8	64.1
	Top floors	142.5	39.6	74.9

$$AE_{max} = max_i \left| y_i^* - y_i \right| \tag{9}$$

$$ARE_{max} = max_i \left| \frac{y_i^* - y_i}{y_i} \right| \tag{10}$$

$$\mathrm{RMSE} = \sqrt{\frac{1}{n} \sum_{i=1}^{n} (y_i^* - y_i)^2} \tag{11}$$

$$\mathrm{CV} = \frac{\mathrm{RMSE}}{\bar{y}} \tag{12}$$

4.2. Results and discussions

4.2.1. Negative rewards in the TDOC

When the optimization was performed every 30 min, the percentages of negative rewards (i.e. the ratio of the number of optimization actions leading to negative reward to the total number of optimization actions) obtained from the TDOC under eight levels of model errors were given in Fig. 6. It was observed that the percentages of negative rewards were very high under all levels of model errors, distributed inside the range between 47.3% and 52.4%. Such high percentages could weaken the overall energy saving potential of the optimal control. When ARE_{max} was decreased from 21.8% (Case 8) to 1.2% (Case 1), there was no obvious reduction in the percentage of negative rewards. The negative reward percentage was as high as 49.4% even in Case 1, which showed that even the model accuracy was high, negative rewards still occurred with a high percentage.

4.2.2. Negative rewards in the TDOC with different optimization frequency

Fig. 7 presents the percentage of negative rewards in these eight cases with four different optimization frequencies: optimization performed at every 15 min, 30 min, 60 min, and 120 min. It was observed that a higher percentage of negative rewards occurred when the optimization was performed every 15 min and 30 min, close to 50% in all eight cases; while it was closed to 30% when the optimization was performed every 60 min and 120 min. In Case 1 to Case 4, the lowest percentage of negative rewards occurred when the optimization was performed every 120 min; while in Case 5 to Case 8, the lowest percentage occurred at the frequency of 60 min.

Fig. 8 shows the energy consumption of the HVAC system under different optimization frequency. As expected, the energy use was the lowest when the optimization frequency was the highest in all eight cases. However, the difference was not significant. For example in Case 1, the energy use was 15,108.2 kWh when the optimization was performed every 15 min, which was reduced by only 0.24% compared with the energy use when the optimization was performed every 120 min. In Case 8, this reduction was 0.19%, still insignificant. Thus, it might not be a good choice to enhance the energy efficiency by using a high optimization frequency since the high percentage of negative rewards in high optimization frequency might discount the potential benefits from the high optimization frequency.

4.2.3. Negative rewards of optimization actions with different Euclidean distances

The Euclidean distance between the optimal values of the decision variables at k and $k-1$, defined by Eqn. (13), was used to quantify how different in the optimal values of the decision variables at two adjacent optimizations. A larger Euclidean indicates a larger difference of the optimal values at k from that at $k-1$. Fig. 9 presented the percentage of negative/positive rewards, where the

Table 4
Model error conditions in these eight cases.

Case#	AE_{max}	ARE_{max}	*RMSE*	*CV*
1	2.277	1.2%	0.898	1.0%
2	3.620	3.3%	1.390	1.5%
3	6.854	5.3%	3.474	3.8%
4	10.034	8.6%	5.836	6.4%
5	15.886	12.9%	8.082	8.8%
6	21.477	14.9%	10.836	11.8%
7	27.272	19.4%	12.676	13.8%
8	36.184	21.8%	17.3	18.8%

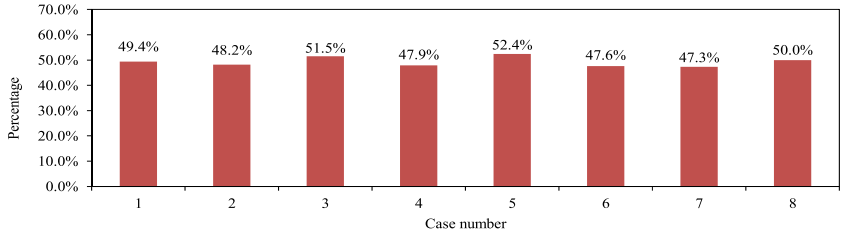

Fig. 6. The percentage of negative rewards in the TDOC when the optimization was performed every 30min under different levels of model errors.

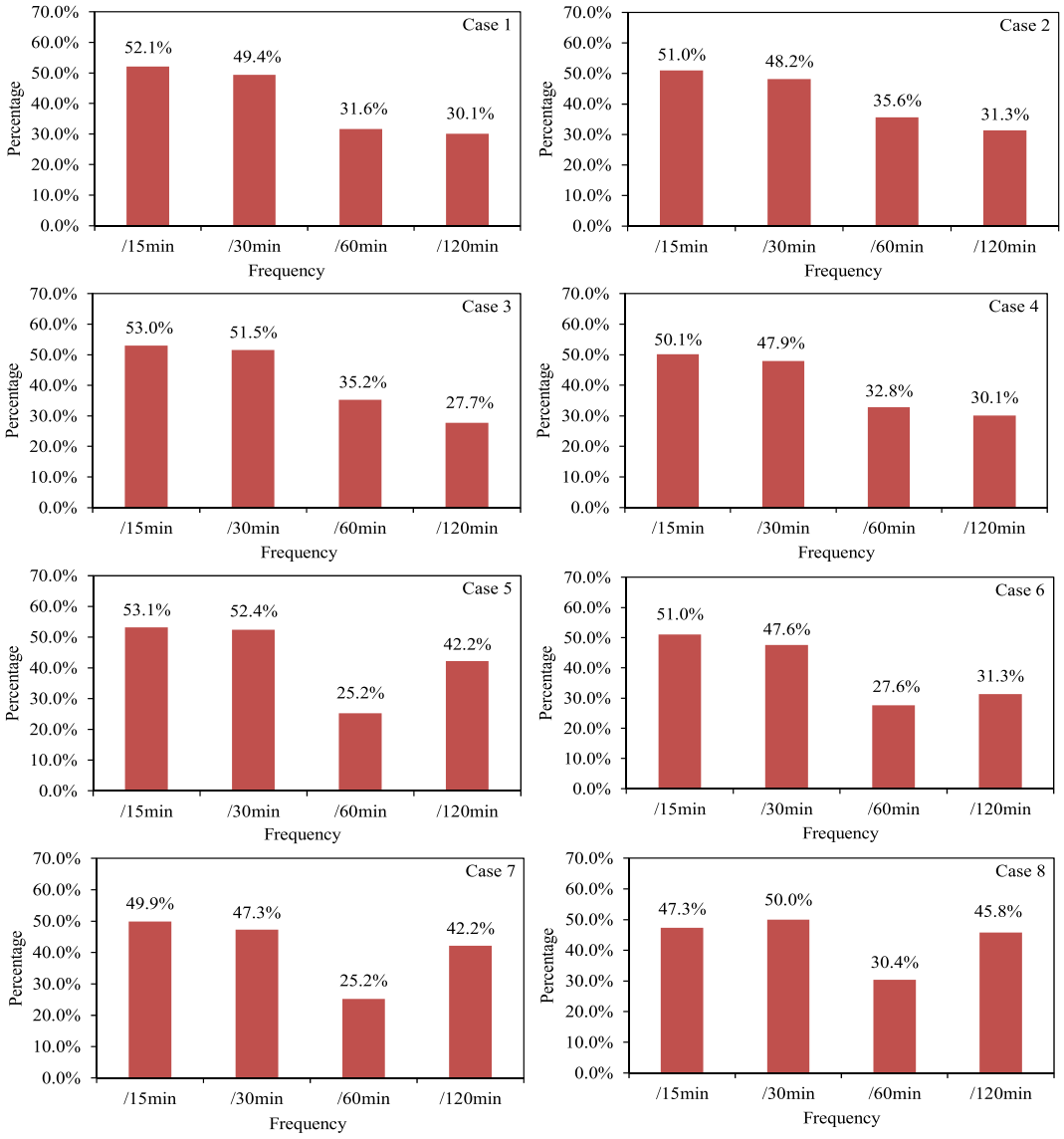

Fig. 7. The percentage of negative rewards in the TDOC under different levels of model errors and different optimization frequencies.

Euclidean distance was divided into seven ranges. When the Euclidean distance was in [0, 0.1]°C, the percentage of negative rewards were around 50% in all eight cases. The increase of Euclidean distance could decrease the percentage of negative rewards. For example, the percentage of negative rewards was 30.6% inside the Euclidean distance between [0.6, 0.9] $^{\circ}C$ in Case 1 and 34.3 in Case 8. This trend was clear under small model-error scale, for example in Case 1. When model error became larger, such as that in Case 8, the percentage of negative reward had no obvious pattern. However, this trend was kept when the average percentage of negative

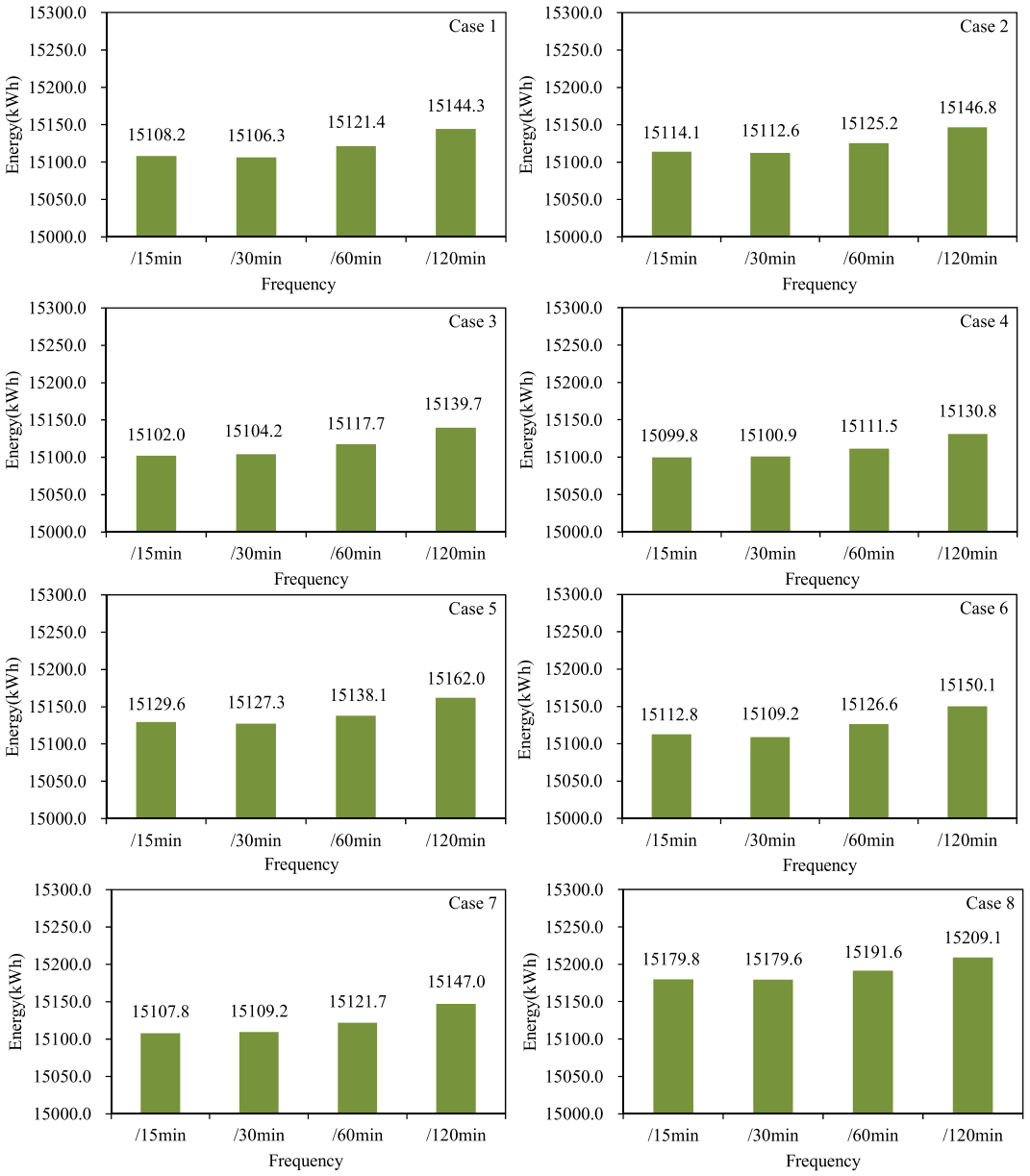

Fig. 8. Energy consumptions in the TDOC under different levels of model errors and different optimization frequencies.

rewards in these eight cases was considered, shown in Table 5.

$$d_{e,k} = \sqrt{\left(T^{opt}_{cw,st,k} - T^{opt}_{cw,st,k-1}\right)^2 + \left(T^{opt}_{chw,st,k} - T^{opt}_{chw,st,k-1}\right)^2 + \left(T^{opt}_{sa,st,k} - T^{opt}_{sa,st,k-1}\right)^2} \tag{13}$$

Fig. 10 was used to explain why a larger Euclidean distance could lead to fewer negative rewards, where a single decision variable v was discussed. At current state S_2, v was optimized and its optimal value was denoted as $v^{opt}_{s_2}$. Assume the optimal value of v at previous step was $v^{opt}_{s_1}$ and the power reduction ΔP_{AB} achieved was negative due to model error. The Euclidean distance between $v^{opt}_{s_1}$ and $v^{opt}_{s_2}$ was indicated by the red double arrow line. When a large Euclidean distance was needed, it was equivalent to move $v^{opt}_{s_1}$ to $v^{opt}_{s_1'}$ (imaging the previous optimization was performed corresponding to the state s_1'). Thus, it was likely to change the negative ΔP_{AB} to a positive $\Delta P_{A'B}$.

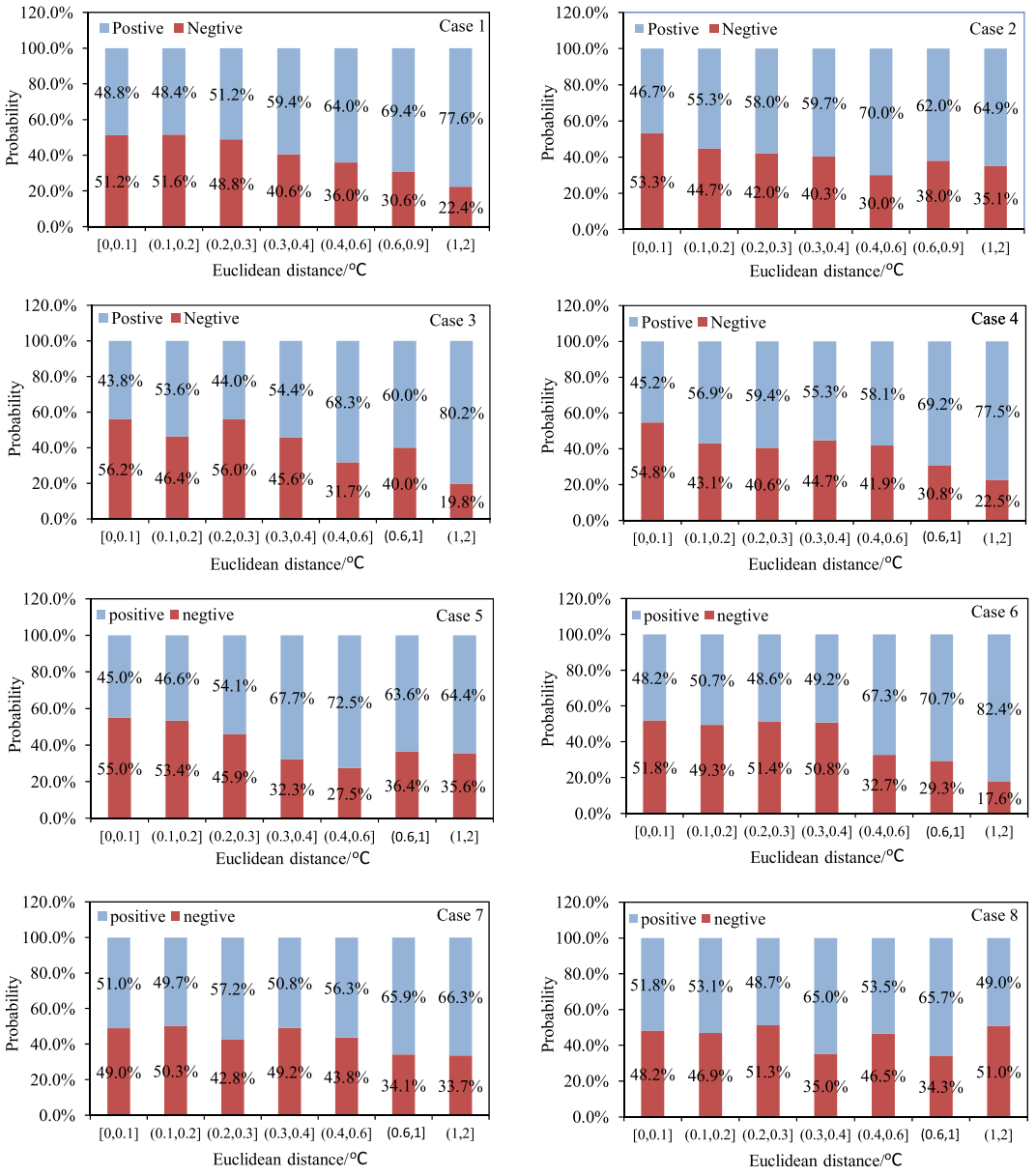

Fig. 9. The percentage of negative and positive optimization rewards in seven ranges of the Euclidean distance for these eight cases.

Table 5
Average percentage of negative rewards in the eight cases.

Euclidean distance section	[0, 0.1]	(0.1, 0.2]	(0.2, 0.3]	(0.3, 0.4]	(0.4, 0.6]	(0.6, 1]	(1, 2]
Average percentage of negative rewards (%)	52.44	48.21	47.35	42.31	36.26	34.19	29.71

5. Impact of model accuracy on event-driven optimal control

5.1. Event definition

Following the work in Hou et al.'s studies [34], an event definition method for the event-driven optimal control was adopted in this study to define events. Using the operation data from Case 1, Case 4, and Case 6 in Section 4, two events were defined to activate the optimization actions in each case, shown in the following equations:

Case 1. (CV = 1.0):

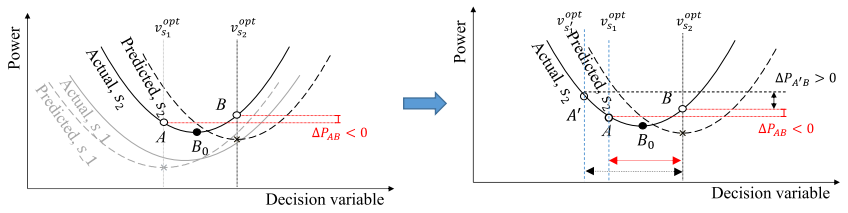

Fig. 10. An example to illustrate the impact of the Euclidean distance on the reward of an optimization action.

$$\begin{cases} e^1: \ |0.764\Delta\Delta T_{wb} - 0.180\Delta\Delta Num_{ch} + 0.330\Delta\Delta PLR + 0.002\Delta\Delta load_{mid}| \geq \gamma \\ e^2: \ |0.330\Delta\Delta T_{wb} - 0.493\Delta\Delta Num_{ch} + 0.888\Delta\Delta PLR - 0.014\Delta\Delta load_{bot} \\ -0.011\Delta\Delta load_{mid} - 0.013\Delta\Delta load_{top}| \geq \gamma \end{cases} \tag{14}$$

Case 4. (CV = 6.4):

$$\begin{cases} e^1: \ |0.786\Delta\Delta T_{wb} - 0.256\Delta\Delta Num_{ch} + 0.004\Delta\Delta load_{mid}| \geq \gamma \\ e^2: \ \begin{vmatrix} 0.243\Delta\Delta T_{wb} - 1.373\Delta\Delta Num_{ch} - 1.003\Delta\Delta PLR \\ -0.012\Delta\Delta load_{bot} - 0.009\Delta\Delta load_{top} \end{vmatrix} \geq \gamma \end{cases} \tag{15}$$

Case 6. (CV = 11.8):

$$\begin{cases} e^1: \ |0.802\Delta\Delta T_{wb} - 0.208\Delta\Delta Num_{ch} + 0.003\Delta\Delta load_{mid}| \geq \gamma \\ e^2: \ |0.356\Delta\Delta T_{wb} - 0.937\Delta\Delta Num_{ch} - 0.014\Delta\Delta load_{bot} - 0.014\Delta\Delta load_{top}| \geq \gamma \end{cases} \tag{16}$$

where ΔT_{db}, ΔT_{wb}, ΔNum_{ch}, ΔPLR, $\Delta load_{bot}$, $\Delta load_{mid}$ and $\Delta load_{top}$ are the changes in the dry-bulb temperature, the wet-bulb temperature, the number of operating chillers, the part-load ratio of the chiller plant, and cooling loads of the bottom, middle and top floors between the current and previous optimization time instant.

The event e^1 was used to activate the optimization of cooling water temperature $T_{cw,st}$ individually; and e^2 was used to drive the optimization of the chilled water temperature $T_{chw,st}$ and the supply air temperature $T_{sa,st}$ simultaneously.

5.2. Event-driven optimal control algorithm

The event-driven RTOC was implemented with the threshold γ being set as 0.3 °C, 0.6 °C, and 0.9 °C respectively for each model-error condition. The time-driven optimal control with the frequency of every 30 min and the operation without optimal control were also carried out for comparison. The search ranges of these three decision variables in both the TDOC and EDOC were set as 1.0 °C. The air conditioning system was operating under these three strategies for a week (Aug. 1 to Aug. 7). The operating conditions were listed in Table 6. Without optimization, these three set-points $T_{cw,st}$, $T_{chw,st}$, and $T_{sa,st}$ were fixed at 30 °C, 7 °C, and 15 °C respectively.

5.3. Results and discussions

5.3.1. Euclidean distance in the EDOC

The Euclidean distances $d_{e,k}$ defined in Eqn. (13) were calculated for the EDOC and TDOC, and their distributions were presented in Fig. 11. It can be observed that the Euclidean distance in the EDOC was generally larger than that in the TDOC and increased with the increase of the threshold γ. For example, when $CV = 1.0$, the Euclidean distance in the TDOC was mainly inside the range of [0, 0.3] °C. The Euclidean distances in the EDOC with the threshold of 0.3 °C, 0.6 °C, or 0.9 °C were mainly inside the range of (0.3, 0.6] °C, (0.6, 0.9] °C, and (0.9, 1.2] °C respectively. The average values of Euclidean distances, $\overline{d}_e$, in the EDOC and TDOC were listed in Table 7 When , the average distance in EDOC with the threshold of 0.3 was increased by 119% compared with the TDOC

5.3.2. Negative rewards in the EDOC

The percentage distributions of negative rewards of all optimization actions in the TDOC and the EDOC were given in Fig. 12. It can be observed that the percentage of negative rewards in the TDOC under three model-error conditions was higher than 42.9%; while that in the EDOCs was inside the range between 5.0% and 26.3% due to larger Euclidean distances obtained. The reason should be the same explained using Fig. 10. Since EDOC optimized the system when events occurred, where events were defined according to the operating condition change of the system, it had a larger Euclidean distance in their optimal values of decision variables and thus reduced the percentage of negative rewards. Thus, EDOCs could indeed reduce the number of optimization actions with negative reward by achieving large Euclidean distances. Besides, because the Euclidean distance in the EDOC increased with the increase of the threshold γ and a larger Euclidean distance led to more positive rewards, a larger threshold in EDOC could help to reduce negative rewards but it is not always tenable. For example, when $CV = 1.0$, the percentage of negative rewards of the EDOC with the threshold of 0.3 °C, 0.6 °C, and 0.9 °C were 26.3%, 11.5%, and 15.4% respectively. Therefore, a threshold of 0.3 °C should be recommended

Table 6
Weather and cooling load condition for the EDOC.

Item		Max.	Min.	Mean
Db temp. (°C)		31.3	25.4	28.0
Wb temp. (°C)		27.2	23.8	25.6
Cooling load (kW)	Bottom	162.4	35.9	84.6
	Middle	116.2	39.1	63.4
	Top	131.2	39.5	64.4

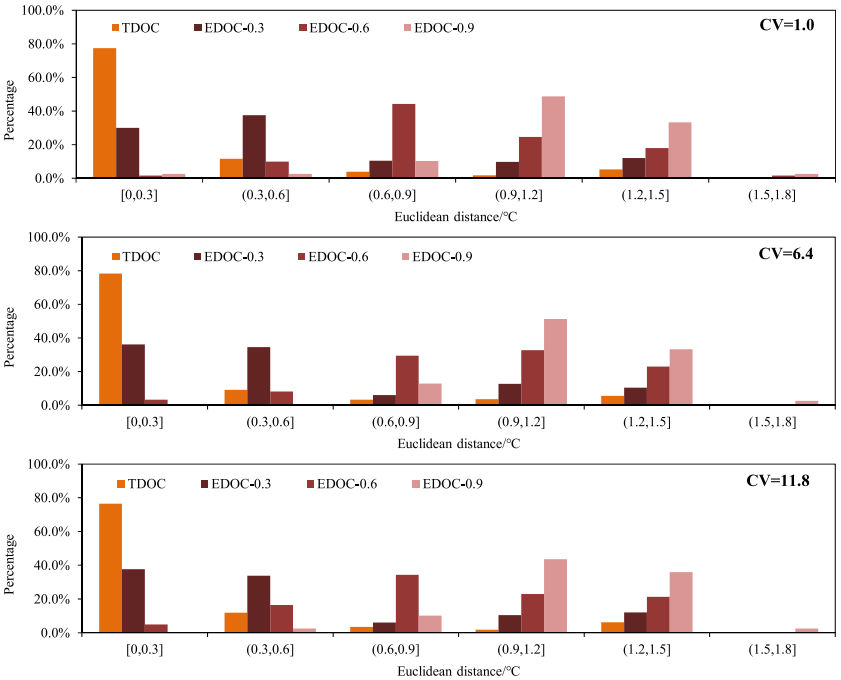

Fig. 11. Percentage distributions of the Euclidean distances in TDOC and EDOC.

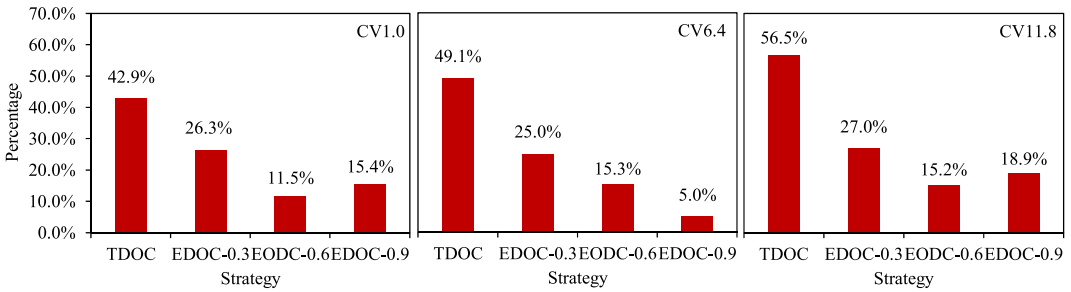

Fig. 12. The percentage distributions of negative rewards of the optimization actions in the TDOC and the EDOC.

considering that it could significantly reduce negative rewards compared with the TDOC.

5.3.3. Computation and energy performance in the EDOC

The computation load of the two optimal control strategies was evaluated by computation time, which was the time spent by the optimization strategies to search for optimal solutions. The profiles of the operating conditions were shown in Fig. 13. The evaluation results were presented in Table 7 as well, which showed that the computation time saving in the EDOC strategy was higher than 67.8% when the TDOC was used as the baseline. The significant saving in the computation load was contributed by the decrease in the number of optimization actions through removing unnecessary optimizations as well as the decrease of the number of decision variables optimized in a single optimization action.

The operation without optimization was used as the baseline to evaluate the energy performance of the TDOC and EDOC. Table 7

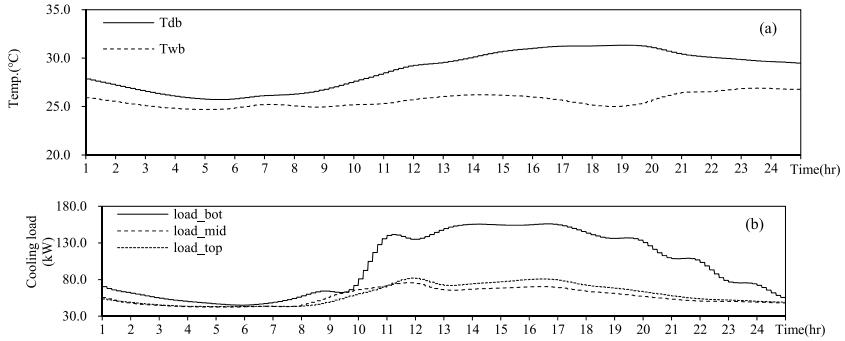

Fig. 13. Profiles of operating conditions on Aug. 1.

Table 7
Evaluation of control strategies.

Case	$\overline{d}_e$ (°C)	Actions ($\Delta P < 0$)	Number of actions	Compute time (s)	Compute saving	Energy (kWh)	Energy saving
No opt.	–	–	–	–	–	15256.3	–
CV=1.0:							
TDOC	0.26	42.9%	336	480.5	–	14444.4	5.3%
EDOC-0.3	0.57	26.3%	133	154.6	67.8%	14451.8	5.3%
EDOC-0.6	0.91	11.5%	61	98.4	79.5%	14450.9	5.3%
EDOC-0.9	1.09	15.4%	39	106.1	77.9%	14497.2	5.0%
CV=6.4:							
TDOC	0.29	49.1%	336	610.0		14434.9	5.4%
EDOC-0.3	0.55	25.0%	140	92.2	84.9%	14440.0	5.4%
EDOC-0.6	0.96	15.3%	59	72.7	88.1%	14460.1	5.2%
EDOC-0.9	1.12	5.0%	40	94.0	84.6%	14472.9	5.1%
CV=11.8:							
TDOC	0.27	56.5%	336	765.4		14451.7	5.3%
EDOC-0.3	0.54	27.0%	141	88.2	88.5%	14455.7	5.3%
EDOC-0.6	0.87	15.2%	66	109.9	85.6%	14457.8	5.2%
EDOC-0.9	1.12	18.9%	37	121.3	84.2%	14536.5	4.7%

presented one-week energy consumptions of all strategies. As shown in Table 7, the EDOC strategies with the threshold of 0.3 °C achieved nearly the same energy performance as the TDOC with the frequency of every 30 min although fewer optimization actions were conducted in the former. There were two reasons. First, the optimization actions in the EDOC with the threshold of 0.3°C were faster in responding the change of operating conditions. Second, fewer negative rewards occurred in the EDOC compared with the TDOC.

Besides, the EDOC with a larger threshold achieved worse energy performance according to Table 7. For example, when $CV = 1.0$, the energy saving in the EDOC with the threshold of 0.3 °C was 5.3% while that in the EDOC with a threshold of 0.9 °C was 5.0%. Fewer

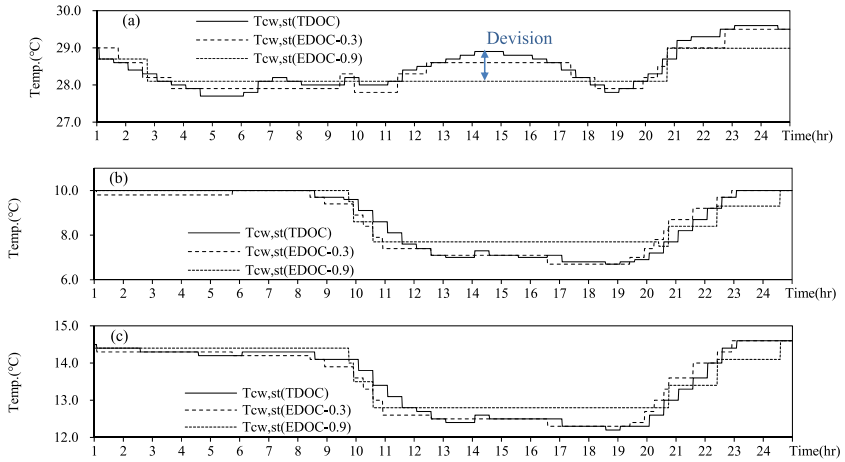

Fig. 14. Profiles of the three temperatures' optimal values on Aug. 1 when $CV = 1.0$.

optimization actions were implemented when a larger threshold was adopted as shown in Table 7 and Fig. 14, which will delay the response to the state changes. Even though the EDOC achieved fewer negative rewards compared with the TDOC, delayed responses to the state changes in the EDOC with a larger threshold, such as 0.9 $^{\circ}C$, could cancel out the benefit brought by reducing the percentage of negative rewards.

6. Conclusion

This paper has investigated the impacts of model accuracy on the optimal control of HVAC systems. The consequence of individual optimization actions has been classified as negative and positive rewards, where the negative reward should be avoided since it could weaken the efficiency of optimization. A series of case studies with different model error scales were carried out to demonstrate the relationship between percentage of negative rewards and the optimization frequency in the TDOC method and the event thresholds in the EDOC method. Through the case studies, it has been found that

- Model errors might lead to a higher percentage in the TDOC of air-conditioning systems and it is not easy to reduce the percentage of negative rewards by increasing the model accuracy. Although decreasing the optimization frequency could help to reduce the percentage of negative rewards, the overall energy-saving effect of the optimal control would be sacrificed in the meanwhile.
- The EDOC strategy could have fewer negative rewards in individual optimization actions compared with the TDOC strategy, thus having better robustness to model errors. A large threshold of events in the EDOC should not be recommended because it cannot always help to reduce negative rewards and might lead to fewer and delayed optimization actions to state changes and thus cancel the energy-saving benefit brought by the decrease of negative rewards. A suitable threshold, such as 0.3 $^{\circ}C$ used in the case studies, could help to achieve comparable energy performance and reduce the computation load significantly compared with the TDOC.

Model error is a long-term challenge for model-based real-time optimal control. Current work was focused on static optimization. When significant thermal storage is used in HVAC systems, dynamic instead of static optimal control strategies should be adopted. Thus, the relationship between model error and optimization reward in dynamic optimization will be the future work.

CRediT authorship contribution statement

Jin Hou: Conceptualization, Methodology, Software, Writing – original draft. **Xin Li:** Writing – review & editingReviewing and Editing. **Hang Wan:** Software, Validation. **Qin Sun:** Visualization, Writing – review & editing. **Kaijun Dong:** Supervision. **Gongsheng Huang:** Conceptualization, Methodology, Supervision, Writing – review & editing.

Declaration of competing interest

The authors declare that they have no known competing financial interests or personal relationships that could have appeared to influence the work reported in this paper.

Acknowledgment

The research work presented in this paper was supported by a grant from the Research Grants Council of the Hong Kong Special Administrative Region, China (CityU 11208918), and a grant from the international cooperation project of Guangzhou Development District (Project No. 2018HG05).

Appendix I

A1. Chiller model

In the DOE2 electric chiller model, the chiller is described by three performance curves: *CapFTemp*, *EIRFTemp*, and *EIRFPLR*. *CapFTemp* is a curve that represents the variation of the cooling capacity as a function of supply temperature of chilled water T_{chws} and supply temperature of cooling water T_{cws}. *EIRFTemp* is a curve that represents the variation of the electric input to cooling output ratio as a function of supply temperature of chilled water T_{chws} and supply temperature of cooling water T_{cws}. *EIRFPLR* is a curve that represents the variation of electric input to cooling output ratio as a function of the part-load ratio of the chiller *PLR*.

$$CapFTemp = a_1 + a_2\Delta T_{chws} + a_3\Delta T_{chws}{}^2 + a_4\Delta T_{cws} + a_5\Delta T_{cws}{}^2 + a_6\Delta T_{chws}\Delta T_{cws} \tag{A1}$$

$$EIRFTemp = b_1 + b_2\Delta T_{chws} + b_3\Delta T_{chws}{}^2 + b_4\Delta T_{cws} + b_5\Delta T_{cws}{}^2 + b_6\Delta T_{chws}\Delta T_{cws} \tag{A2}$$

$$EIRFPLR = c_1 + c_2\Delta PLR + c_3\Delta PLR \tag{A3}$$

where the Part-load ratio *PLR* is defined as

$$PLR = load/Q_{avail} \tag{A4}$$

$$Q_{avail} = Q_{ref}\Delta CapFTemp \tag{A5}$$

The chiller power is given by

$$P_{chiller} = \frac{Q_{ref}}{COP_{ref}} \Delta\ CapFTemp \Delta EIRFTemp \Delta EIRFPLR \tag{A6}$$

where COP_{ref} is the chiller's reference coefficient of performance; Q_{ref} is the chiller's reference capacity, kW. The return temperature of chilled water T_{cwr} is given by

$$T_{cwr} = T_{cws} + \frac{load + P_{chiller}}{C_{pw} \Delta m_{cw}} \tag{A7}$$

where m_{cw} is the mass flow rate of cooling water, kg/s; C_{pw} is the specific heat of water under constant pressure, kJ/(kg·K). Regression coefficients to describe the three curves are listed in the following table.

Table 1
Regression coefficients in the chiller model.

Symbol	Value	Symbol	Value	Symbol	Value
a_1	1.002148	b_1	0.4475957	c_1	0.2519108
a_2	0.03300191	b_2	−0.01054652	c_2	0.2756914
a_3	0.000374167	b_3	0.000712687	c_3	0.4725826
a_4	0.005925358	b_4	0.01158632		
a_5	−0.0000259927	b_5	0.000515151		
a_6	−0.0002172126	b_6	−0.0009831355		

A2. Cooling tower model

The heat taken away by the air in the cooling tower $Q_{ct,a}$ can be calculated according to

$$Q_{ct,a} = m_a \Delta \left(h_{a,out} - h_{a,in}\right) \tag{A8}$$

where m_a is air mass flow rate, kg/s; $h_{a,in}$ is air enthalpy at the cooling tower inlet, kJ/kg; and $h_{a,out}$ is air enthalpy at the cooling tower outlet, kJ/kg. This model relies on an assumption that the leaving air of the cooling tower is saturated and its temperature equal to the actual leaving temperature. Then, the heat taken away by the air in the cooling tower and the equivalent specific heat of air $C_{pa,fi}$ can be calculated by

$$Q_{ct,a} = m_a \Delta C_{pa,fi} \Delta \left(T_{awb,out} - T_{awb,in}\right) \tag{A9}$$

$$C_{pa,fi} = \left(h_{a,out} - h_{a,in}\right) / \left(T_{awb,out} - T_{awb,in}\right) \tag{A10}$$

Where $T_{awb,in}$ is inlet air temperature, $^{\circ}C$; $T_{awb,out}$ is leaving air temperature, $^{\circ}C$. Based on the ε-*NTU* method, the cooling tower effectiveness can be obtained by

$$\varepsilon_{fi} = \left[1 - e^{-NTU\Delta(1-\omega)}\right] / \left[1 - \omega \Delta e^{-NTU\Delta(1-\omega)}\right] \tag{A11}$$

The number of transfer units *NTU* and the ratio of the minimum heat capacity flow rate to the maximum heat capacity flow rate ω can be expressed by

$$NTU = AU_{fi} / C_{min} \tag{A12}$$

$$\omega = C_{min} / C_{max} \tag{A13}$$

where $C_{min} = \min(C_w, C_{fi})$, $C_{max} = \max(C_w, C_{fi})$; and AU_{fi} is an equivalent heat transfer coefficient-area product, kW/K. C_{min} and C_{max} are the minimum and maximum capacity flow rate, which were determined by $C_{fi} = C_{pa,fi} \bullet m_a$ and $C_w = C_{pw} \bullet m_{cw}$, where C_{pw} is the specific heat of water under constant pressure, kJ/(kg·K); m_{cw} is the mass flow rate of the cooling water, kg/s.

The relationship between the equivalent heat transfer coefficient-area product AU_{fi} and the actual heat transfer coefficient-area product *AU* is shown as follows:

$$AU_{fi} = AU \bullet C_{pa,fi} / C_{pa} \tag{A14}$$

where C_{pa} is the specific heat of the air under constant pressure, kJ/(kg·K). The relationship of the actual heat transfer coefficient-area product *AU* and the mass flow rate of the air m_a and the cooling water m_{cw} is

$$AU = D_0 \bullet \left(m_{cw} / m_{cw,des}\right)^n \bullet \left(m_a / m_{a,des}\right)^m \tag{A15}$$

where $m_{cw,des}$ is the mass flow rate of cooling water under design condition, kg/s; $m_{a,des}$ is the mass flow rate of air under design

condition, kg/s; D_0, m, and n are coefficients to be identified

The total heat transferred between the air and the cooling water in the cooling tower $Q_{a,w}$ and the total heat transferred on the water-side $Q_{a,w}$ can be calculated by

$$Q_{a,w} = \varepsilon_{fi} \bullet C_{min} \bullet \left(T_{cwr} - T_{awb,in}\right) \tag{A16}$$

$$Q_{ct,w} = C_{pw} \bullet \dot{m}_{cw} \bullet \left(T_{cwr} - T_{cws}\right) \tag{A17}$$

where $Q_{ct,w}$ is heat transferred on the water-side, kW; T_{cwr} is inlet cooling water temperature of the cooling tower, $^{\circ}C$; and T_{cws} is outlet cooling water temperature of the cooling tower, $^{\circ}C$.

The power of the cooling tower fan $P_{fan,CT}$ is calculated by

$$P_{fan,CT} = P_{fan,des} \bullet \left(V_a / V_{a,des}\right)^3 \tag{A18}$$

where $V_a = m_a/Density$; and $Density$ is given by

$$Density = 1.293 - 0.003023 \bullet T_{awb,in} - 0.002849 \cdot T_{awb,wb,in} \tag{A19}$$

where $P_{fan,des}$ is fan power under design condition, kW; V_a is air volume flow rate, m^3/s; $V_{a,des}$ is air volume flow rate under design condition, m^3/s; $Density$ is the air density, kg/m^3. $T_{awb,wb,in}$ is the inlet air web bulb temperature, $^{\circ}C$. In the cooling tower model, there are three coefficients D_0, m and n to be identified by the method of the genetic algorithm using operating data. Design parameters and identified parameters are shown in the following table.

Table 2
Design and identified parameters for the cooling tower.

Symbol	Value	Symbol	Value
$\dot{m}_{cw,des}$	27	D_0	51.48
$\dot{m}_{a,des}$	23	m	0.7695
$V_{a,des}$	18	n	1
P_{design}	5		

A3. AHU model

The heat transfer model of the AHU coil adopted here uses a user-specified bypass fraction to describe the heat exchange performance. It is assumed that a fraction of the air stream bypasses the coil and the remainder exits the coil. The two air streams are mixed after the coil. Outlet air of the cooling coil is at a saturated condition and its temperature $T_{a,\ out}$ is calculated by

$$T_{a,\ out} = \left(T_{chw,\ in} + T_{chw,out}\right)/2 \tag{A20}$$

where $T_{chw,\ in}$ is the inlet temperature of chilled water, $^{\circ}C$; $T_{chw,out}$ is the out temperature of chilled water, $^{\circ}C$. The temperature $T_{a,\ mix}$ and moisture content $W_{a,\ mix}$ of the mixed air stream after the coil are as follows.

$$T_{a,\ mix} = \left(1 - f_{bypass}\right) \bullet T_{a,out} + f_{bypass} \bullet T_{a,\ in} \tag{A21}$$

$$W_{a,\ mix} = \left(1 - f_{bypass}\right) \bullet W_{a,out} + f_{bypass} \bullet W_{a,\ in} \tag{A22}$$

where f_{bypass} is the fraction bypass the cooling coil in AHU, and 0.15 is adopted here; $T_{a,\ in}$ is the inlet air temperature, $^{\circ}C$; $W_{a,\ in}$ is the inlet air moisture content, $kgH_2O/kgAir$; and $W_{a,out}$ is the outlet air moisture content, $kgH_2O/kgAir$.

The heat transfer on the air side Q_{air} is calculated by

$$Q_{air} = m_a \bullet \left(1 - f_{bypass}\right) \bullet \left(h_{a,\ in} - h_{a,out}\right) \tag{A23}$$

where m_a is the total air mass flow rate (including bypass air), kg/s; $h_{a,\ in}$ is the inlet air enthalpy, kJ/kg; $h_{a,out}$ is the outlet air enthalpy, kJ/kg. The temperature T_{cond} and amount m_{cond} of condensate are $T_{cond} = T_{a,\ out}$ and $m_{cond} = m_a \bullet (1 - f_{bypass}) \bullet (W_{a,\ out} - W_{a,in})$ respectively. The heat transfer on the water side Q_w is calculated by

$$Q_w = m_a \bullet \left(1 - f_{bypass}\right) \bullet \left(h_{a,\ in} - h_{a,out}\right) - m_{cond} \bullet h_{cond} \tag{A24}$$

where h_{cond} is the outlet water enthalpy, kJ/kg. The outlet chilled water temperature is

$$T_{chw,out} = Q_w / m_{chw} / C_{pw} + T_{chw,in} \tag{A25}$$

m_{chw} is the mass flow rate of chilled water, kg/s; C_{pw} is the specific heat of water under constant pressure, kJ/(kg·K).

The power of the AHU fan $P_{fan,\ AHU}$ is calculated by

$$P_{fan,AHU} = P_{fan,AHU,des} \bullet \left(m_a / m_{a,des}\right)^3 \tag{A26}$$

where $P_{fan,AHU,des}$ is fan power under design condition, kW; m_a is air mass flow rate, kg/s; and $m_{a,des}$ is air mass flow rate under design condition, kg/s.

Table 3
Design parameters for the AHU.

Symbol	AHU at Bottom	AHU at Middle	AHU Top
$P_{fan,AHU,des}$	18.5	7	10
$m_{a,des}$	10	7	8

A4. Pump model (variable speed pump)

Pump power P_{pump} is calculated by

$$P_{pump} = P_{pump,des} \bullet \left(m_w / m_{w,des}\right)^3 \tag{A27}$$

where $P_{pump,des}$ is pump power under design condition, kW (18 is adopted for the chilled water pump); m_w is water mass flow rate, kg/s; and $m_{w,des}$ is water mass flow rate under design condition, kg/s (46 is adopted for the chilled water pump).

References

[1] ASHRAE Handbook, ASHRAE Handbook - HVAC Applications, SI Edition, ASHRAE, Atlanta, 2019.
[2] C.P. Underwood, HVAC Control Systems: Modeling, Analysis and Design, E & FN Spon, London & New York, 1999.
[3] J. Singh, N. Singh, J.K. Sharma, Fuzzy modeling and control of HVAC systems - a review, J. Sci. Ind. Res. 65 (2006) 470–476.
[4] Y. Yao, D.K. Shekhar, State of the art review on model predictive control (MPC) in Heating Ventilation and Air-conditioning (HVAC) field, Build. Environ. 200 (2021) 107952.
[5] G.S. Huang, K.V. Ling, X. Xu, Y. Liao, Generalized eigenvalue minimization for uncertain first-order plus time-delay processes, ISA Trans. 53 (2014) 141–149.
[6] K. Chua, S. Chou, W. Yang, J. Yan, Achieving better energy-efficient air conditioning–a review of technologies and strategies, Appl. Energy 104 (2013) 87–104.
[7] S.W. Wang, Z.J. Ma, Supervisory and optimal control of building HVAC systems: a review, HVAC R Res. 14 (2008) 3–32.
[8] Z. Cumali, Global optimization of HVAC system operations in real time, Build. Eng. 94 (1988) 1729–1744.
[9] M.M. Haghighi, A.L. Sangiovanni-Vincentelli, Modeling and Optimal Control Algorithm Design for HVAC Systems in Energy Efficient Buildings, Masters report, 2011.
[10] A. Kusiak, M.Y. Li, F. Tang, Modeling and optimization of HVAC energy consumption, Appl. Energy 87 (2010) 3092–3102.
[11] N. Nassif, S. Kajl, R. Sabourin, Optimization of HVAC control system strategy using two-objective genetic algorithm, HVAC R Res. 11 (2005) 459–486.
[12] S.A. Hussain, G.S. Huang, R.K.K. Yuen, W. Wang, Adaptive regression model-based real-time optimal control of central air-conditioning systems, Appl. Energy 276 (2020) 115427.
[13] K.F. Fong, V.I. Hanby, T.T. Chow, HVAC system optimization for energy management by evolutionary programming, Energy Build. 38 (2006) 220–231.
[14] Y.C. Chang, F.A. Lin, C.H. Lin, Optimal chiller sequencing by branch and bound method for saving energy, Energy Convers. Manag. 46 (2005) 2158–2172.
[15] M. Zaheer-Uddin, G. Zheng, Optimal control of time-scheduled heating, ventilating and air conditioning processes in buildings, Energy Convers. Manag. 41 (2000) 49–60.
[16] H.C. Spindler, L.K. Norford, Naturally ventilated and mixed-mode buildings part II: optimal control, Build. Environ. 44 (2009) 750–761.
[17] Z. Afroz, G. Shafiullah, T. Urmee, G. Higgins, Modeling techniques used in building HVAC control systems: a review, Renew. Sustain. Energy Rev. 83 (2018) 64–84.
[18] S.W. Wang, X.Q. Jin, Model-based optimal control of VAV air-conditioning system using genetic algorithm, Build. Environ. 35 (2000) 471–487.
[19] Z.J. Ma, S.W. Wang, An optimal control strategy for complex building central chilled water systems for practical and real-time applications, Build. Environ. 44 (2009) 1188–1198.
[20] Y. Zhang, V.I. Hanby, Model-based control of renewable energy systems in buildings, HVAC R Res. 12 (2006) 739–760.
[21] J. Li, G. Poulton, G. Platt, J. Wall, G. James, Dynamic zone modelling for HVAC system control, Int. J. Model. Ident. Control 9 (2010) 5–14.
[22] K. Amarasinghe, D. Wijayasekara, H. Carey, M. Manic, D. He, W.P. Chen, Artificial neural networks based thermal energy storage control for buildings, in: IECON the 41st Annual Conference of the, IEEE Industrial Electronics Society, 2015, pp. 5421–5426.
[23] A. Afram, F. Janabi-Sharifi, A.S. Fung, K. Raahemifar, Artificial neural network (ANN) based model predictive control (MPC) and optimization of HVAC systems: a state of the art review and case study of a residential HVAC system, Energy Build. 141 (2017) 96–113.
[24] Z.J. Ma, S.W. Wang, Supervisory and optimal control of central chiller plants using simplified adaptive models and genetic algorithm, Appl. Energy 88 (2011) 198–211.
[25] H.S. Asad, R.K.K. Yuen, J. Liu, J. Wang, Adaptive modeling for reliability in optimal control of complex HVAC systems, Build. Simul. 12 (2019) 1095–1106.
[26] S.H. Kim, G. Augenbroe, Uncertainty in developing supervisory demand-side controls in buildings: a framework and guidance, Autom. ConStruct. 35 (2013) 28–43.
[27] P. Huang, Y. Wang, Y.J. Sun, G.S. Huang, Review of uncertainty-based design methods of central air-conditioning systems and future research trends, Sci. Technol. Built Environ. 25 (2019) 819–835.
[28] A.S. Potts, R.A. Romano, C. Garcia, Improving performance and stability of MPC relevant identification methods, Control Eng. Pract. 22 (2014) 20–33.
[29] S. Kolathaya, A.D. Ames, Parameter to state stability of control Lyapunov functions for hybrid system models of robots, Nonlinear Anal.: Hybrid Syst. 25 (2017) 174–191.
[30] J. Baccou, J.Z. Zhang, P. Filion, G. Damblin, et al., Development of good practice guidance for quantification of thermal-hydraulic code model input uncertainty, Nucl. Eng. Des. 354 (2019) 110173.
[31] S. Liu, G.P. Henze, Impact of modeling accuracy on predictive optimal control of active and passive building thermal storage inventory, Build. Eng. 110 (2004) 151.
[32] W. Jiang, T.A. Reddy, P. Gurian, General methodology combining engineering optimization of primary HVAC&R plants with decision analysis methods - Part II: uncertainty and decision analysis, HVAC R Res. 13 (2007) 119–140.
[33] J.Q. Wang, G.S. Huang, Y.J. Sun, X.P. Liu, Event-driven optimization of complex HVAC systems, Energy Build. 133 (2016) 79–87.

[34] J. Hou, X. Luo, G.S. Huang, L. Zhang, Z. Yu, M. Eftekhari, Development of event-driven optimal control for central air-conditioning systems, J. Build. Performance Simul. 13 (2020) 378–390.
[35] J. Široký, F. Oldewurtel, J. Cigler, S. Prívara, Experimental analysis of model predictive control of an energy efficient building heating system, Appl. Energy 88 (2011) 3079–3087.
[36] B. Lehmann, D. Gyalistras, M. Gwerder, K. Wirth, S. Carl, Intermediate complexity model for model predictive control of integrated room automation, Energy Build. 58 (2013) 250–262.
[37] J. Wang, Q.S. Jia, G.S. Huang, Y. Sun, Event-driven optimal control of central air-conditioning systems: event-space establishment, Sci. Technol. Built Environ. 24 (2018) 839–849.
[38] Commercial prototype building models, available at https://www.energycodes.gov/prototype-building-models.
[39] EnergyPlus weather format, available at https://designbuilder.co.uk/cahelp/Content/EnergyPlusWeatherFileFormat.htm.
[40] M. Hydeman, K.L. Gillespie, A. Dexter, Tools and techniques to calibrate electric chiller component models, Build. Eng. 108 (2002) 733–741.
[41] J. Lebrun, C.A. Silva, F. Trebilcock, E. Winandy, Simplified models for direct and indirect contact cooling towers and evaporative condensers, Build. Serv. Eng. Technol. 25 (2004) 25–31.
[42] TESS handbook, TESS COMPONENT LIBRARIES general descriptions, available at http://www.trnsys.com/tess-libraries/TESSLibs17_General_Descriptions.pdf.
[43] F. Tahmasebi, A. Mahdavi, A two-staged simulation model calibration approach to virtual sensors for building performance data, in: Proceedings of the 13th Conference of International Building Performance Simulation Association, Chambéry, France, 2013, pp. 25–28.
[44] G. Mustafaraj, J. Chen, G. Lowry, Thermal behaviour prediction utilizing artificial neural networks for an open office, Appl. Math. Model. 34 (2010) 3216–3230.
[45] S. Soyguder, H. Alli, Predicting of fan speed for energy saving in HVAC system based on adaptive network based fuzzy inference system, Expert Syst. Appl. 36 (2009) 8631–8638.
[46] A. Kusiak, G. Xu, Modeling and optimization of HVAC systems using a dynamic neural network, Energy 42 (2012) 241–250.
[47] K. Li, H. Su, J. Chu, Forecasting building energy consumption using neural networks and hybrid neuro-fuzzy system: a comparative study, Energy Build. 43 (2011) 2893–2899.